Numerical Investigation of a Berthed Engineering Ship Subjected to Narrow-Gap Resonance

Zhiyang Zhang[1,2], Xingyu Pan[2], Ziheng Wang[2], Weixing Liu[1,2] and Haitao Wu[3,*]

[1] School of Ocean Engineering, Jiangsu Ocean University, Lianyungang, 222005, China

[2] Makarov College of Marine Engineering, Jiangsu Ocean University, Lianyungang, 222005, China

[3] Department of Naval Architecture, Ocean and Marine Engineering, University of Strathclyde, Glasgow, G4 0LZ, UK

Revista Internacional
Métodos numéricos
para cálculo y diseño en ingeniería
RIMNI
UNIVERSITAT POLITÈCNICA
DE CATALUNYA
BARCELONATECH
In cooperation with
CIMNE

INFORMATION

Keywords:
Berthed engineering ship
narrow-gap resonance
hydrodynamic interactions
damping lid method
gumbel distribution
extreme load response

DOI: 10.23967/j.rimni.2025.10.74047

Revista Internacional de Métodos Numéricos para Cálculo y Diseño en Ingeniería

Numerical Investigation of a Berthed Engineering Ship Subjected to Narrow-Gap Resonance

Zhiyang Zhang[1,2], **Xingyu Pan**[2], **Ziheng Wang**[2], **Weixing Liu**[1,2] **and Haitao Wu**[3,*]

[1]School of Ocean Engineering, Jiangsu Ocean University, Lianyungang, 222005, China

[2]Makarov College of Marine Engineering, Jiangsu Ocean University, Lianyungang, 222005, China

[3]Department of Naval Architecture, Ocean and Marine Engineering, University of Strathclyde, Glasgow, G4 0LZ, UK

ABSTRACT

This paper investigates the hydrodynamic behavior of a berthed engineering ship using a potential model incorporating the damping lid method, which effectively mitigates the strong hydrodynamic interactions caused by narrow-gap resonance. First, the viscous correction approach is validated against experimental data. Then, the abrupt variations in the ship's hydrodynamic characteristics at resonant frequencies are analyzed for different gap widths. Subsequently, by comparing the ship motion responses obtained from the response amplitude operators (RAOs) and the Cummins equation, the damping factors at specific frequencies are identified. Finally, under severe sea-state conditions, a safety assessment of the mooring system is performed. The results reveal that narrower gaps lead to stronger hydrodynamic interactions. Moreover, the predicted extreme load responses confirm that the mooring system is capable of ensuring the ship's safety. This study provides useful insights for the design of berthed structures with narrow gaps.

OPEN ACCESS

Received: 30/09/2025

Accepted: 21/11/2025

DOI
10.23967/j.rimni.2025.10.74047

Keywords:
Berthed engineering ship
narrow-gap resonance
hydrodynamic interactions
damping lid method
gumbel distribution
extreme load response

1 Introduction

For purposes such as cargo loading and unloading, maintenance, and resupply, ships are required to be moored alongside coastal or offshore berths. In recent years, an increasing number of offshore berthing facilities have been established to meet specific operational demands [1,2]. However, due to their exposure to open seas and the absence of effective shielding structures, ships moored at these facilities face elevated risks of damage to mooring components under complex marine environmental conditions [3,4]. Consequently, particular attention must be devoted to the accurate simulation of environmental loads and the rational design of mooring systems.

Against this backdrop, numerous scholars have investigated the hydrodynamic behavior of moored ships. Shen et al. [5] conducted experimental studies on an oil tanker moored at a pier, examining the interactions between the mooring system and incident waves. Their results revealed

---

*Correspondence: Haitao Wu (haitao.wu@strath.ac.uk).

that the breast lines experienced the highest tension within the system. Ziylan and Nas [6] proposed a quasi-static method for the mooring analysis of berthed ships and validated it through a series of analyses. They found that the method yielded results with less than 3% error, demonstrating its strong practical value. Wen et al. [7] experimentally evaluated a multi-buoy-assisted mooring system designed for bulk carriers and showed that this novel configuration effectively prevented the breakage of mooring lines and fenders while reducing the ship's motion amplitudes. Wan et al. [8] investigated the influence of various fender designs and material properties on the performance of a floating storage tank under both regular and 100-year-return-period irregular wave conditions, further performing a parametric analysis of viscous effects. Considering harbor resonance, Yan et al. [9] assessed the impact of different mooring arrangements and pretension levels on the dynamic response of berthed ships. Their results indicated that moderately increasing pretension effectively reduced mooring line tension and that deploying multiple lines on a single bollard improved the tension distribution. Zhu et al. [10] performed both numerical and experimental studies on the hydrodynamic response of moored ships under long-period swell conditions, finding that surge and heave responses were mainly governed by the swell period, whereas roll and pitch responses were primarily influenced by the ship's intrinsic characteristics.

In moored systems with closely spaced bodies, a phenomenon known as narrow-gap resonance may occur when the fluid within the gap interacts with incoming waves of specific frequencies. The frequencies associated with this phenomenon, termed gap-resonant frequencies, include both piston and sloshing modes [11]. In the piston mode, the gap fluid moves collectively in an up-and-down motion, whereas in the sloshing mode, it oscillates back and forth. Once gap resonance is triggered, the wave-induced loads on the structures and the fluid elevation within the gap can be significantly amplified [12–15], posing potential threats to the integrity of the berthed system. Under such conditions, analyzing the mechanism of gap resonance in multi-body configurations becomes essential.

Extensive research has been conducted on gap resonance in multi-body systems through theoretical analyses, experimental investigations, and numerical simulations. Theoretical studies have primarily focused on deriving analytical formulations to estimate gap-resonant frequencies [16,17]. Experimental investigations can generally be divided into two categories: two-dimensional (2D) tests conducted in wave flumes [18,19] and three-dimensional (3D) tests conducted in wave basins [20,21]. These experiments aim to enhance understanding of the underlying physical mechanisms of gap resonance and to provide benchmark data for validating numerical simulations. Among the available approaches, numerical simulations are the most widely employed, typically based on either computational fluid dynamics (CFD) or potential flow methods. The CFD approach, which solves the Navier–Stokes equations and explicitly accounts for fluid viscosity, can accurately reproduce gap resonance phenomena [22,23]. However, the complexity of parameter settings and the high computational cost limit its applicability in practical engineering. In contrast, potential flow models offer significant advantages in efficiency and simplicity. Although potential models tend to overestimate resonance amplitudes due to the neglect of viscous effects, they can still accurately predict resonance frequencies. Consequently, the incorporation of viscous corrections into potential models to improve the prediction accuracy of gap resonance has become an active area of research.

Currently, potential models with artificial damping are commonly adopted to enhance the accuracy of predicting gap-resonant behavior in multi-body systems. Several damping implementations have been proposed [24–26], including the damping lid, flexible mat, and viscous dissipation term. Zhao et al. [27] employed potential models incorporating these three damping approaches to investigate gap resonance in a fixed twin-barge system, finding good agreement between the numerical predictions and experimental measurements for both resonance amplitudes and frequencies. Similarly, Watai et al. [28] demonstrated that introducing artificial damping into potential models improves convergence in time-domain simulations. It should be noted, however, that resonance behavior depends on factors such as the hydrodynamic properties of the floating bodies, the frequencies of the incident waves, and the gap width. Therefore, the damping coefficients employed in artificial damping methods must be determined case by case [29].

Although extensive studies have been conducted on berthed ships, most have focused on mooring design, analytical methods, and wave conditions, as summarized above. In contrast, the effects of gap resonance on moored ships have received limited attention. It should be emphasized that at certain frequencies, inaccurate prediction of ship motion responses may arise due to insufficient suppression of strong hydrodynamic interactions, potentially threatening the safety of the mooring system. This paper therefore focuses on examining the impact of gap resonance on the dynamic performance of a berthed engineering ship. The damping lid method is employed for viscous correction, and appropriate damping factors are determined to improve predictive accuracy. Finally, the safety of the moored ship is evaluated by computing the extreme loads acting on the mooring system. The findings of this study are expected to provide valuable insights for the design and assessment of similar offshore berthing systems.

2 Theoretical Background

This study performs a hydrodynamic analysis of a berthed system consisting of an engineering ship and a fixed dock structure. The hydrodynamic coefficients and wave forces acting on the ship are computed using three-dimensional potential flow theory in conjunction with the boundary element method (BEM). Because potential flow theory neglects viscous damping, the hydrodynamic characteristics of the ship may exhibit abrupt variations near piston or sloshing resonance frequencies when a narrow gap is present. In such cases, the omission of viscous damping corrections can lead to inaccuracies in time-domain simulations, making it difficult to reliably estimate the load responses of mooring lines and fenders near resonance frequencies. This uncertainty may pose safety risks to the ship under severe sea conditions. To address this issue, a viscous correction approach known as the damping lid method is adopted. As illustrated in Fig. 1, this method introduces an artificial lid at the mean water level (MWL) between the ship and dock, with a width corresponding to that of the gap. The core concept of the damping lid method is to modify the free-surface boundary condition in the gap region by introducing a damping-related term, thereby accounting for viscous energy dissipation. The subsequent sections describe the underlying potential flow model, the BEM formulation, and the time-domain Cummins equation.

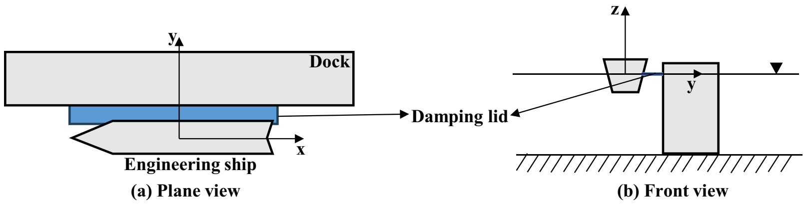

(a) Plane view (b) Front view

Figure 1: Schematic diagram of the damping lid between the dock and engineering ship

2.1 Potential Model

The potential theory assumes that the fluid is inviscid, irrotational, and incompressible, and the velocity potential Φ is composed of the incident potential φ_i, diffraction potential φ_d and radiation potential φ_{rj} [30],

$$\Phi(x,y,z,t) = Re\left\{\left[(\varphi_i + \varphi_d) + \sum_{j=1}^{6} \varphi_{rj}^{(1)}\xi_j^{(1)}\right]e^{-i\omega t}\right\} \tag{1}$$

where: the superscript (1) denotes the engineering ship; $\xi_j^{(1)}$ is the velocity amplitude of the ship in the j-th degree of freedom (DOF). It should be noted that since the dock is fixed, it does not generate any radiation potential. Furthermore, the incident potential is written as:

$$\varphi_i = -\frac{iA_\omega g}{\omega}\frac{\cosh[k(z+h)]}{\cosh(kh)}e^{ik(x\cos\beta + y\sin\beta)} \tag{2}$$

$$k = \frac{\omega^2}{g\tanh(k\mathrm{h})} \tag{3}$$

where: A_ω, ω and β represent the wave amplitude, angular frequency and incident direction, respectively; g is the gravity acceleration; k is the wave number; h is the water depth.

Regarding the boundary value problems for the diffraction and radiation potentials, the following boundary conditions should be satisfied [31,32],

$$\begin{cases} in\,\Omega:\ \Delta\varphi_d = 0 \\ on\,S_F:\ -\dfrac{\omega^2}{g}\varphi_d + \dfrac{\partial\varphi_d}{\partial z} = 0 \\ on\,S_0:\ \dfrac{\partial\varphi_d}{\partial n} = -\dfrac{\partial\varphi_i}{\partial n},\ S_0 = S_1 + S_2 \\ on\,S_B:\ \dfrac{\partial\varphi_d}{\partial n}|_{z=-\mathrm{h}} = 0 \\ on\,S_\infty:\ \lim_{r\to\infty}\sqrt{r}\left(\dfrac{\partial\varphi_d}{\partial r} - ik\varphi_d\right) = 0 \end{cases} \tag{4}$$

$$\begin{cases} in\,\Omega:\ \Delta\varphi_{rj}^{(1)} = 0 \\ on\,S_F:\ -\dfrac{\omega^2}{g}\varphi_{rj}^{(1)} + \dfrac{\partial\varphi_{rj}^{(1)}}{\partial z} = 0 \\ on\,S_m:\ \dfrac{\partial\varphi_{rj}^{(1)}}{\partial n^{(m)}} = \begin{cases} -i\omega n_j^{(1)},\ \mathrm{m} = 1 \\ 0,\ \mathrm{m} = 2 \end{cases} \\ on\,S_B:\ \dfrac{\partial\varphi_{rj}^{(1)}}{\partial n}|_{z=-\mathrm{h}} = 0 \\ on\,S_\infty:\ \lim_{r\to\infty}\sqrt{r}\left(\dfrac{\partial\varphi_{rj}^{(1)}}{\partial r} - ik\varphi_{rj}^{(1)}\right) = 0 \end{cases} \tag{5}$$

where: Ω denotes the fluid domain; S_F, S_B, and S_∞ represent the free surface, seabed, and far-field boundaries, respectively. When $m = 1$ and 2, S_m corresponds to the wetted surfaces of the ship and dock, respectively, while S_0 denotes the total wetted surfaces of both bodies. Indeed, the free-surface boundary conditions in Eqs. (4) and (5) do not consider viscous corrections. To address this issue, the free-surface boundary equations based on the damping lid method are employed [33],

$$\frac{\omega^2}{g}\left(\alpha^2 f-1\right)\varphi_d-2i\frac{\omega^2}{g}\alpha^2 f\varphi_d+\frac{\partial\varphi_d}{\partial z}=0 \tag{6}$$

$$\frac{\omega^2}{g}\left(\alpha^2 f-1\right)\varphi_{rj}^{(1)}-2i\frac{\omega^2}{g}\alpha^2 f\varphi_{rj}^{(1)}+\frac{\partial\varphi_{rj}^{(1)}}{\partial z}=0 \tag{7}$$

where: α represents the damping factor, and the value of f can be determined by the formulas,

$$f=\begin{cases}\sin^2\left(\dfrac{\pi\omega}{2\omega_0}\right), & \omega<\omega_0\\ \left(\dfrac{\omega}{\omega_0}\right)^2, & \omega\geq\omega_0\end{cases} \tag{8}$$

$$\omega_0=\max\left\{0.1,\sqrt{\frac{\pi g}{d_{gap}}}\right\} \tag{9}$$

Generally, α is within the range of [0, 1]. When $\alpha=0$, the free-surface boundary conditions are the same with those without the viscous correction. When $\alpha=1$, the free surface is treated as a rigid lid, implying that no wave elevation occurs within the gap. Notably, $\alpha=0.2$ can be considered as a heavy damping factor.

After obtaining the diffraction and radiation potentials using the BEM, the hydrodynamic pressure acting on the wetted surface of the ship is resolved by the linearized Bernoulli formula. Subsequently, by integrating the pressure over the wetted surface, the first-order wave force in j-th DOF is derived as:

$$F_j^{(1)}=\iint_{S_1}pn_j^{(1)}ds=i\omega\rho e^{-i\omega t}\iint_{S_1}(\varphi_i+\varphi_d)n_j^{(1)}ds \tag{10}$$

where: ρ denotes the seawater density.

Meanwhile, the radiation forces on the wetted surface of the ship can similarly be expressed as:

$$\begin{aligned}\mathrm{F}_{\mathrm{rjk}}^{(1)}&=\mathrm{i}\omega\rho\iint_{\mathrm{S}_1}\left\{\mathrm{Re}\left[\varphi_{\mathrm{rk}}^{(1)}\right]+\mathrm{iIm}\left[\varphi_{\mathrm{rk}}^{(1)}\right]\right\}\mathrm{n}_{\mathrm{j}}^{(1)}\mathrm{ds}=-\omega\rho\iint_{\mathrm{S}_1}\mathrm{Im}\left[\varphi_{\mathrm{rk}}^{(1)}\right]\mathrm{n}_{\mathrm{j}}^{(1)}\mathrm{dS}+\mathrm{i}\omega\rho\iint_{\mathrm{S}_0}\mathrm{Re}\left[\varphi_{\mathrm{rk}}^{(1)}\right]\mathrm{n}_{\mathrm{j}}^{(1)}\mathrm{ds}\\&=\omega^2\mathrm{A}_{\mathrm{jk}}^{(1)}+\mathrm{i}\omega\mathrm{B}_{\mathrm{jk}}^{(1)}\end{aligned} \tag{11}$$

$$A_{jk}^{(1)}=-\frac{\rho}{\omega}\iint_{S_1}Im\left[\varphi_{rk}^{(1)}\right]n_j^{(1)}ds \tag{12}$$

$$B_{jk}^{(1)}=\rho\iint_{S_1}Re\left[\varphi_{rk}^{(1)}\right]n_j^{(1)}ds \tag{13}$$

where: $F_{rjk}^{(1)}$ denotes the radiation forces in the j-th DOF induced by unit motion of the ship in the k-th DOF; $A_{jk}^{(1)}$ and $B_{jk}^{(1)}$ represent the added mass and radiation damping in the j-th DOF, respectively, induced by unit motion in the k-th DOF.

After obtaining the hydrodynamic coefficients and wave forces of the ship, its equation of motion in the frequency domain is written as:

$$\sum_{j=1}^{6}[-\omega^2(M_{ij}^{(1)}+A_{ij}^{(1)})+i\omega B_{ij}^{(1)}+K_{ij}^{(1)}]\eta_j^{(1)}=F_i^{(1)},i=1,2,\ldots,6 \tag{14}$$

where: $M_{ij}^{(1)}$ and $K_{ij}^{(1)}$ represent the mass and hydrostatic stiffness matrices of the ship, respectively; $\eta_j^{(1)}$ represents the RAO in the j-th DOF. According to the Ref. [33], approximately 5%–10% of the critical damping is typically applied to consider the viscous roll damping. Regarding the critical damping, it is derived as:

$$B_{critical,4}^{(1)} = 2\sqrt{(I_{xx} + \Delta I_{xx})K_{roll}} \tag{15}$$

The method to convert the RAOs into the time-domain responses is commonly utilized to validate the Cummins model under free-floating conditions [33].

$$\eta_{rao,j}^{(1)}(t) = A_w {*} Re\left[\eta_j^{(1)}(i\omega)e^{-i\omega t}\right] \tag{16}$$

In the presence of narrow gap, the resonance frequencies of the ship corresponding to the piston mode and sloshing mode can be estimated with the empirical equations [34,35],

$$\omega_p = \sqrt{\frac{g}{\frac{d_{gap}{*}B}{\mathrm{h} - d} + d}} \tag{17}$$

$$\omega_{s,n} = \sqrt{\frac{g\pi n}{d_{gap}}}, n = 1, 2, 3\ldots \tag{18}$$

where: d and B are the draft and width of the ship, respectively; n denotes the n-th sloshing mode.

Under real sea conditions, the ship is not only subjected to first-order wave excitation but also second-order wave excitation. Based on the near-field approach proposed by Pinkster, the second-order wave excitation is formulated as [36]:

$$\begin{gathered}F_j^{(2)} = -\frac{1}{2}\rho g \oint_{wl^{(1)}} \zeta_r^{(1)} \cdot \zeta_r^{(1)} n_j^{(1)} dl + \frac{1}{2}\rho \iint\limits_{S_1} \left[\nabla\Phi^{(1)} \cdot \nabla\Phi^{(1)}\right] n_j^{(1)} ds + \rho \iint\limits_{S_1} \left[X^{(1)} \cdot \nabla\frac{\partial\Phi^{(1)}}{\partial t}\right] n_j^{(1)} ds + \\ \Theta^{(1)} \times F^{(1)} + \rho \iint\limits_{S_1} \frac{\partial\Phi^{(2)}}{\partial t} n_j^{(1)} ds\end{gathered} \tag{19}$$

where: $wl^{(1)}$ denotes the ship's waterline; $\zeta_r^{(1)}$ is the relative wave elevation; $X^{(1)}$ and $\Theta^{(1)}$ represent the first-order translational and rotational displacements of the ship, respectively; $F^{(1)}$ represents the total first-order hydrodynamic forces; $\Phi^{(1)}$ and $\Phi^{(2)}$ denote first-order and second-order velocity potentials, respectively.

Under irregular wave conditions, the second-order wave excitation induced by a pair of waves with $\left(A_j, \omega_j, \alpha_j\right)$ and $(A_k, \omega_k, \alpha_k)$ can be calculated using Pinkster's approximation method [36],

$$\begin{cases} F_{jk}^{(2)}(t) = \mathrm{Re}\left\{F_{jk}^{(2)} e^{-i\left(\omega_j - \omega_k\right)t + i\left(\alpha_j - \alpha_k\right)}\right\} \\ F_{jk}^{(2)} = f_{jk} F^{(1)}\left(k_j - k_k\right) \end{cases} \tag{20}$$

where: A_j and A_k denote the amplitudes of the j-th and k-th wave components, respectively; α_j and α_k represent the phases of the j-th and k-th wave components; $F^{(1)}\left(k_j - k_k\right)$ are the first-order wave excitation induced by a wave with unit amplitude and wave number $\left(k_j - k_k\right)$. In addition, the variable f_{jk} can be expressed as:

$$f_{jk} = \frac{A_j A_k L_{jk}\left(\omega_j - \omega_k\right)}{g} \tag{21}$$

where:

$$L_{jk} = \frac{1}{2}g^2 \frac{C_{jk} + D_{jk}}{\left(\omega_j - \omega_k\right)^2 - \left(k_j - k_k\right) g \tanh\left(k_j - k_k\right) \mathrm{h}} \tag{22}$$

$$C_{jk} = \frac{k_j^2}{\omega_j \cosh^2 k_j \mathrm{h}} - \frac{k_k^2}{\omega_k \cosh^2 k_k \mathrm{h}} \tag{23}$$

$$D_{jk} = \frac{2k_j k_k \left(\omega_j - \omega_k\right)\left(1 + \tanh k_j \mathrm{h} \tanh k_k \mathrm{h}\right)}{\omega_j \omega_k} \tag{24}$$

Finally, under finite water depth, the velocity potential is resolved using the BEM and the frequency-domain pulsating Green function [37,38].

2.2 Time-Domain Cummins Equation of Motion

After obtaining the hydrodynamic coefficients and wave excitation forces of the engineering ship, these quantities are transformed into time-domain expressions using inverse Fourier transforms. Additionally, the ship operates under the combined effects of wind, waves, and current, and is constrained by mooring lines and fenders. Therefore, based on the Cummins model, the time-domain motion equation of the ship is derived as [39]:

$$\begin{aligned}&\sum_{j=1}^{6}\left[M_{ij}+A_{ij}(\infty)\right]\ddot{x}_j(t)+\int_0^t \mathrm{h}_{ij}(t-\tau)\dot{x}_j(\tau)d\tau+B_{vis,ij}\dot{x}_j(t)+K_{ij}x_j(t) = \\ &F_{w1,i}(t)+F_{w2,i}(t)+F_{w,i}(t)+F_{c,i}(t)+F_{m,i}(t)+F_{f,i}(t)\end{aligned} \tag{25}$$

where: $A_{ij}(\infty)$ is the added mass at infinite frequency; $\mathrm{h}_{ij}(t)$ is the retardation function implying fluid memory effects [40]; $B_{vis,ij}$ is the corrected viscous damping term, as introduced in the frequency-domain model; $F_{w1,i}$ and $F_{w2,i}$ are the first-order and second-order wave forces, respectively; $F_{w,i}$ and $F_{c,i}$ denote the wind and current loads; $F_{m,i}$ and $F_{f,i}$ represent the mooring force and fender contact force, respectively. It is noted that in the current study, the polyester rope and rubber are employed to simulated the mooring lines and fenders, respectively. The corresponding formulas for $h_{ij}(t)$, $A_{ij}(\infty)$, $F_{w,i}$, $F_{c,i}$, F_m and F_f are derived as:

$$\mathrm{h}_{ij}(t) = \frac{2}{\pi}\int_0^\infty B_{ij}(\omega)\cos(\omega t)d\omega \tag{26}$$

$$A_{ij}(\infty) = A_{ij}(\omega) + \frac{1}{\omega}\int_0^\infty h_{ij}(\tau)\sin(\omega\tau)d\tau \tag{27}$$

$$F_{w,i}(t) = \frac{1}{2}\rho_a C_{wd,i} S_w V_{rw}^2 \tag{28}$$

$$F_{c,i}(t) = \frac{1}{2}\rho C_{cd,i} S_c V_{rc}^2 \tag{29}$$

$$F_m(t) = K_m \delta_m \tag{30}$$

$$F_f(t) = K_{f1}\delta_f + K_{f2}\delta_f^2 \tag{31}$$

where: ρ_a is the air density; $C_{wd,i}$ and $C_{cd,i}$ are the wind and current force coefficients, respectively; S_w and S_c represent the projected areas in the wind and current directions; V_{rw} and V_{rc} denote the relative wind and current velocities, respectively; K_m and δ_m are the stiffness and elongation of the mooring line. Concerning the fender, the polynomial function is utilized to simulate the nonlinear relationship between the contact forces and compression, where K_{f1} and K_{f2} are the coefficients, and

δ_f is the compression. Furthermore, the detailed simulation of the fenders could be found in [41]. As for the first- and second-order wave loads acting on the ship, these are calculated based on the wave spectrum [42]. In this study, the JONSWAP spectrum is employed to represent irregular wave conditions.

3 Validation of Damping Lid Method

This study adopts the twin-barge system reported in Ref. [43] as a benchmark case to validate the damping lid method, as illustrated in Fig. 2. The principal properties of the full-scale twin-barge system are summarized in Table 1. After developing the boundary element model (BEM) of the twin-barge system incorporating the damping lid, a series of frequency-domain simulations are performed. Fig. 3 compares the response amplitude operators (RAOs) of Barge 1 in the heave and pitch degrees of freedom (DOFs) between the numerical results obtained in this study and the experimental data from Ref. [43]. The results clearly show that the motion responses near the resonance frequencies are substantially suppressed by the application of damping, while the influence on other frequency ranges remains minimal. Furthermore, among the tested damping factors, the results obtained with $\alpha = 0.02$ exhibit good agreement with the experimental observations. These findings demonstrate that, when an appropriate damping factor is adopted, the implementation of a damping lid can effectively enhance the predictive accuracy of motion response simulations for floating bodies.

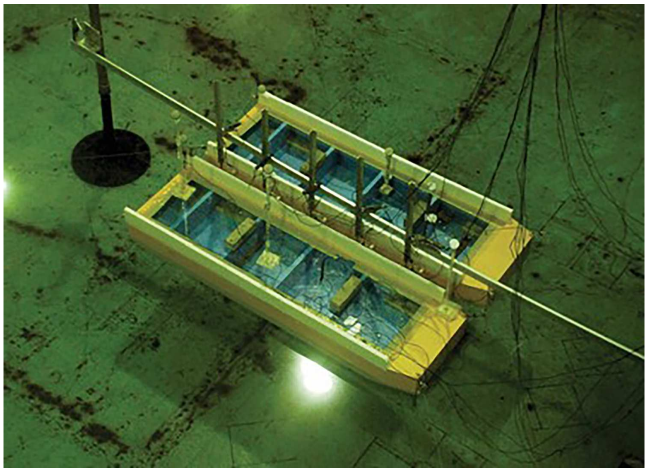

Figure 2: Illustration of the model-scale twin-barge system [43]

Table 1: Main properties of the full-scale twin-barge system

Property	Unit	Value
Length	m	90
Breadth	m	27
Draft	m	4
Distance between barges	m	6
Water depth	m	42

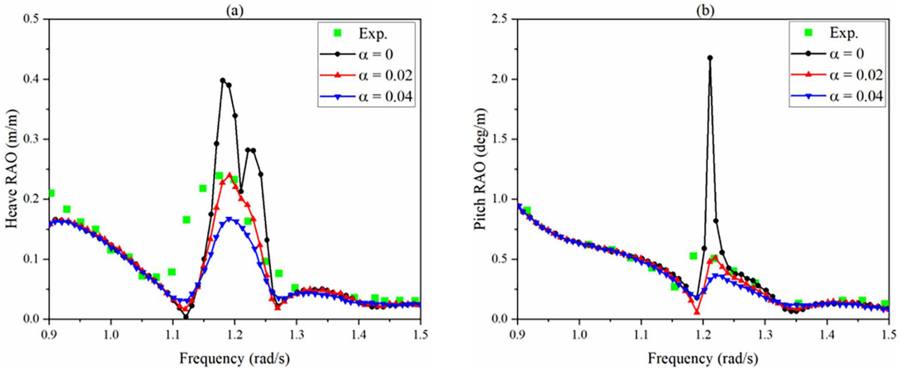

Figure 3: Comparisons of the RAOs of Barge 1 with $d_{gap} = 6$ m between the numerical and experimental results: (**a**) Heave DOF; (**b**) Pitch DOF

4 Characteristics of Berthed System

This paper investigates a berthed system comprising an engineering ship and a dock structure, as illustrated in Fig. 4. The principal parameters of the system are summarized in Table 2. Furthermore, the theoretical resonance frequencies for the piston and sloshing modes at different gap widths are calculated using Eqs. (17) and (18) and presented in Table 3. Because these formulas are derived under the deep-water assumption, the calculated values may contain slight discrepancies. In addition, the frequency interval adopted in the present study is not sufficiently fine, which may cause the numerical simulations to miss the exact resonance frequencies. Nevertheless, the resonance frequencies listed in Table 3 still serve as useful references for analyzing the variation trends of the hydrodynamic characteristics across different gap widths.

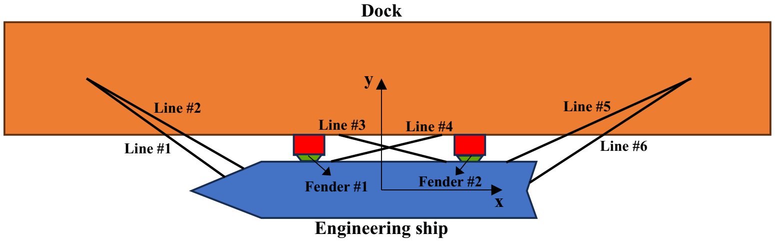

Figure 4: Schematic diagram of the berthing system

Table 2: Main parameters of the engineering ship, dock, and mooring system

	Property	Unit	Value
Engineering ship	Length	m	76
	Breadth	m	20.4
	Draft	m	5.6
	Longitudinal center of gravity relative to forward perpendicular	m	38.7
	Vertical center of gravity relative to MWL	m	2.2
	Roll radius of gyration	m	7.3

(Continued)

Table 2 (continued)

	Property	Unit	Value
	Pitch radius of gyration	m	22.6
	Yaw radius of gyration	m	22.5
	Displacement	kg	$6.479E^6$
Dock	Length	m	200
	Breadth	m	20
	Depth relative to MSL	m	20
Mooring line	Number	–	6
	Diameter	mm	100
	Weight in air	kg/m	5000
	Axial stiffness	kN	1180
	Minimum breaking load	kN	$1.639E^6$
Fender	Number	–	2
	Thickness	m	0.5
	Coefficients of the polynomial function	–	$3E^6/1E^7$
	Maximum allowable load	kN	$4.905E^6$

Table 3: Theoretical piston-mode and sloshing-mode resonant frequencies of the engineering ship for different gap widths

Gap width (m)	Piston-mode frequency (rad/s)	1st-order sloshing-mode frequency (rad/s)	2nd-order sloshing-mode frequency (rad/s)
3	1.058	–	–
5	0.950	2.482	–
9	0.806	1.850	2.616

5 Results and Discussion

The present study investigates the application of the damping lid approach to a multi-body hydrodynamic model. It is noted that all frequency-domain analyses presented in the subsequent sections are performed within a wave frequency range of 0.05 to 2.7 rad/s, with an interval of 0.05 rad/s. In addition, a mesh convergence analysis of the berthing system is conducted prior to the formal simulations. Fig. 5 compares the sway steady drift forces of the berthed system at the incident direction of 90° between far-field method and near-field method. From the figure, it can be observed that the results of steady drift force under near-field method agree well with those under far-field method, which verifies the mesh convergence of the numerical model [44]. Finally, the numbers of quadrilateral panels for the dock and ship are determined to be 13,240 and 2608, respectively.

5.1 Hydrodynamic Interactions at Different Gap Widths

The hydrodynamic interactions among multi-body structures can be effectively characterized through their hydrodynamic coefficients. Figs. 6 and 7 present the comparisons of the added mass and radiation damping of the engineering ship at various gap widths. The results show that, in the single-body scenario, the hydrodynamic coefficient curves are relatively smooth. In contrast, the coefficients in the ship–dock system exhibit distinct oscillations. Moreover, for all degrees of freedom (DOFs), the oscillation amplitudes are most pronounced at a gap width of 3 m, indicating that smaller gaps lead to stronger hydrodynamic interactions.

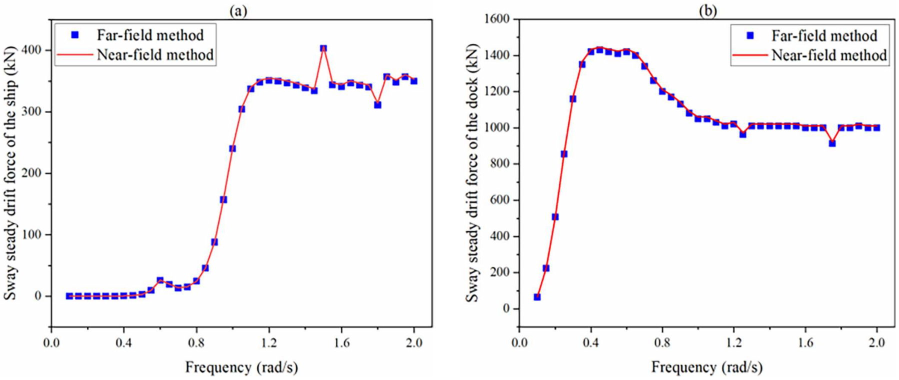

Figure 5: Comparison of sway steady drift forces between far-field method and near-field method: (**a**) ship; (**b**) dock

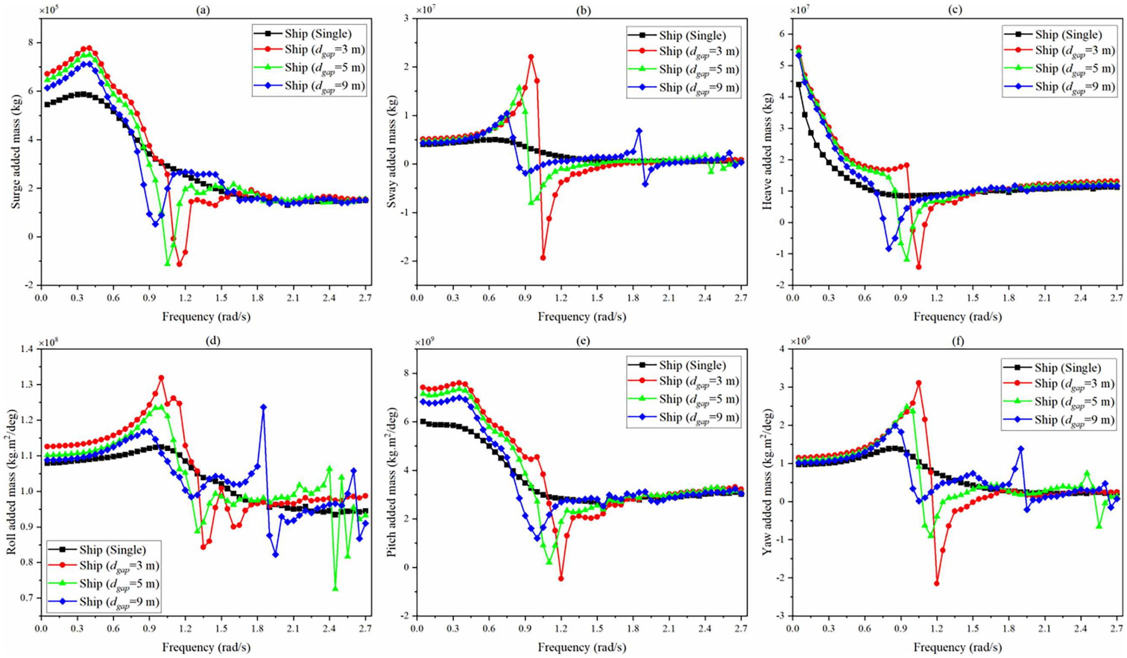

Figure 6: Added mass of the ship in six DOFs at various gap widths

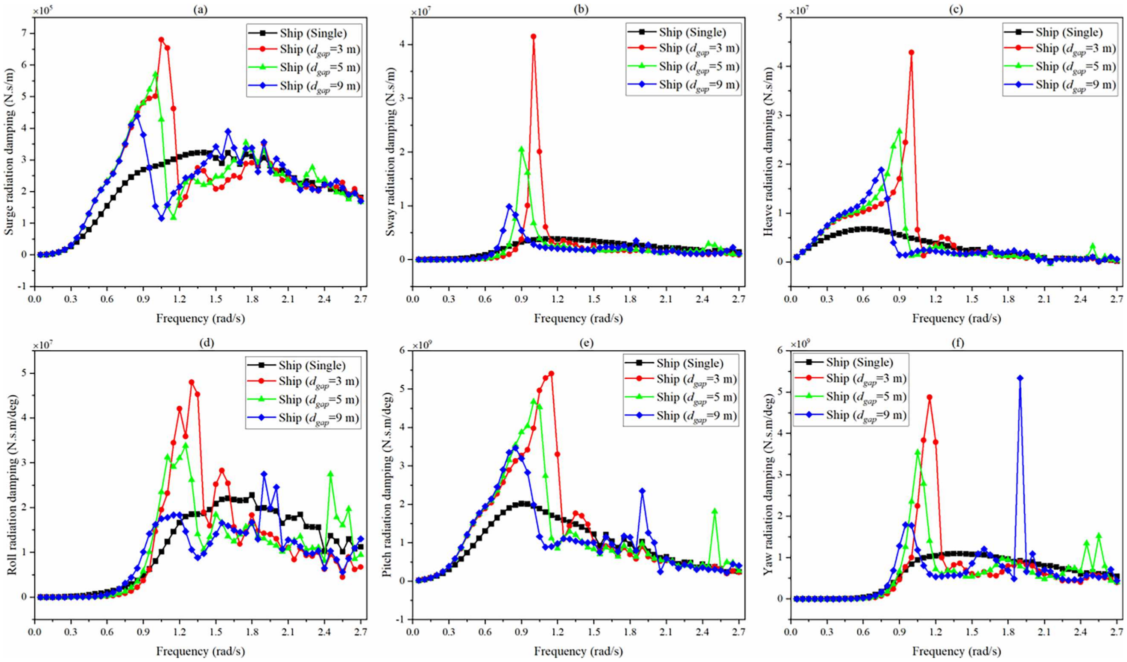

Figure 7: Radiation damping of the ship in six DOFs at various gap widths

As shown in Fig. 6a,c,e, the surge, heave, and pitch added masses display only the piston-mode resonance within the frequency range, with the resonance frequency decreasing as the gap width increases. Additionally, for these three DOFs, the added mass shows a decreasing and then increasing trend near the resonance frequency. From Fig. 6b,d,f, it is evident that the sway, roll, and yaw added masses exhibit only piston-mode resonance at $d_{gap} = 3$ m. However, when the gap width exceeds 3 m, the sloshing modes also appear for these DOFs. Specifically, at $d_{gap} = 5$ m, only the first-order sloshing resonance is observed, while at $d_{gap} = 9$ m, both first- and second-order sloshing modes are present. It is noteworthy that the first-order sloshing resonance frequency at $d_{gap} = 5$ m is significantly higher than that at $d_{gap} = 9$ m, but still lower than the second-order sloshing frequency at $d_{gap} = 9$ m. Furthermore, for $d_{gap} = 9$ m, the added mass at the first-order sloshing frequency is larger than that at the second-order sloshing frequency. Additionally, in the vicinity of the resonance frequencies, the added mass for these three DOFs exhibits a pattern of increasing, then decreasing, and then increasing again. From Fig. 6a–f, it is also demonstrated that in presence of gap resonance, the added mass becomes negative in some cases, a phenomenon not present in the single-body case.

As shown in Fig. 6a,c,e, the surge, heave, and pitch added masses exhibit only piston-mode resonance within the investigated frequency range, with the resonance frequency decreasing as the gap width increases. For these three DOFs, the added mass decreases and then increases near the resonance frequency. From Fig. 6b,d,f, it is evident that the sway, roll, and yaw added masses display only piston-mode resonance at $d_{gap} = 3$ m. However, when the gap width exceeds 3 m, sloshing modes also emerge for these DOFs. Specifically, at $d_{gap} = 5$ m, only the first-order sloshing resonance appears, whereas at $d_{gap} = 9$ m, both first- and second-order sloshing modes are present. It is noteworthy that the first-order sloshing resonance frequency at $d_{gap} = 5$ m is significantly higher than that at $d_{gap} = 9$ m, yet remains lower than the second-order sloshing frequency at $d_{gap} = 9$ m. Furthermore, for $d_{gap} = 9$ m, the added mass corresponding to the first-order sloshing frequency is larger than that of the second-order mode. Near the resonance frequencies, the added mass for these DOFs shows a characteristic pattern of increasing, decreasing, and then increasing again. Fig. 6a–f also reveals that, in the presence of gap resonance, the added mass becomes negative in certain cases—a phenomenon absent in the single-body scenario.

Fig. 7 infers that the variation patterns of radiation damping at different gap widths are more complex than those of the added mass. In particular, the surge and roll radiation damping display highly oscillatory behavior due to narrow-gap resonance. Nevertheless, similar to the added mass, all six DOFs exhibit piston-mode resonance in their radiation damping curves. In Fig. 7a, sharp fluctuations in surge radiation damping indicate strong piston-mode resonance across all gap widths. Fig. 7d further shows that, in addition to piston-mode resonance, the roll radiation damping also exhibits first-order sloshing resonance when the gap width exceeds 3 m. As seen in Fig. 7b,c, the sway and heave radiation damping respond to the first-order sloshing frequency at $d_{gap} = 5$ m, though with relatively small oscillation amplitudes. Similarly, Fig. 7e,f demonstrate that the pitch and yaw radiation damping display first-order sloshing resonance when the gap width exceeds 3 m. Notably, at $d_{gap} = 9$ m, the yaw radiation damping at the first-order sloshing frequency is significantly larger than that at the piston-mode resonance frequency, implying that the sloshing mode dominates the yaw radiation damping for this configuration.

5.2 Hydrodynamic Analysis with Different Damping Factors

In this study, $d_{gap} = 5$ m is selected as the operating condition for investigating the damping lid method, serving also as a preparatory step for the subsequent analyses. Zou et al. [45] emphasized that selecting an appropriate damping factor is crucial for obtaining reliable results when using the damping lid approach. Therefore, this subsection performs a parametric analysis of the damping factor with respect to the hydrodynamic characteristics of the ship, focusing on the sway, heave, and roll degrees of freedom (DOFs). Figs. 8–10 illustrate the hydrodynamic coefficients, wave excitation forces, and response amplitude operators (RAOs) of the ship under different damping factors, respectively. From these figures, it can be inferred that the damping lid method is effective in suppressing narrow-gap resonance in the hydrodynamic responses. Furthermore, the damping effects become more pronounced at the piston and first-order sloshing resonance modes as the damping factor increases.

As shown in Fig. 8a,c, near the first-order sloshing resonance frequency, the sway and roll added masses for $\alpha = 0.05$ differ noticeably from those without viscous correction. However, once viscous damping is introduced, the variations in added mass among different damping factors become relatively small. Figs. 7f and 8e indicate that, for the heave radiation damping, the suppressive effect of the damping lid at the sloshing resonance is less significant than that at the piston resonance, whereas for the yaw radiation damping, the damping effects are evident at both resonance frequencies.

Fig. 9 presents the wave excitation on the ship under a wave heading of 90°. It can be observed that, compared with the sway and roll DOFs, the influence of the damping lid on the heave DOF is relatively minor. Notably, the roll wave excitation exhibits strong oscillations beyond the piston resonance frequency due to narrow-gap resonance. Moreover, with viscous correction applied, the variation of roll wave forces with respect to the damping factor becomes more complex. Nevertheless, the overall damping effects on roll wave excitation generally intensify as the damping factor increases, particularly around the piston and first-order sloshing frequencies.

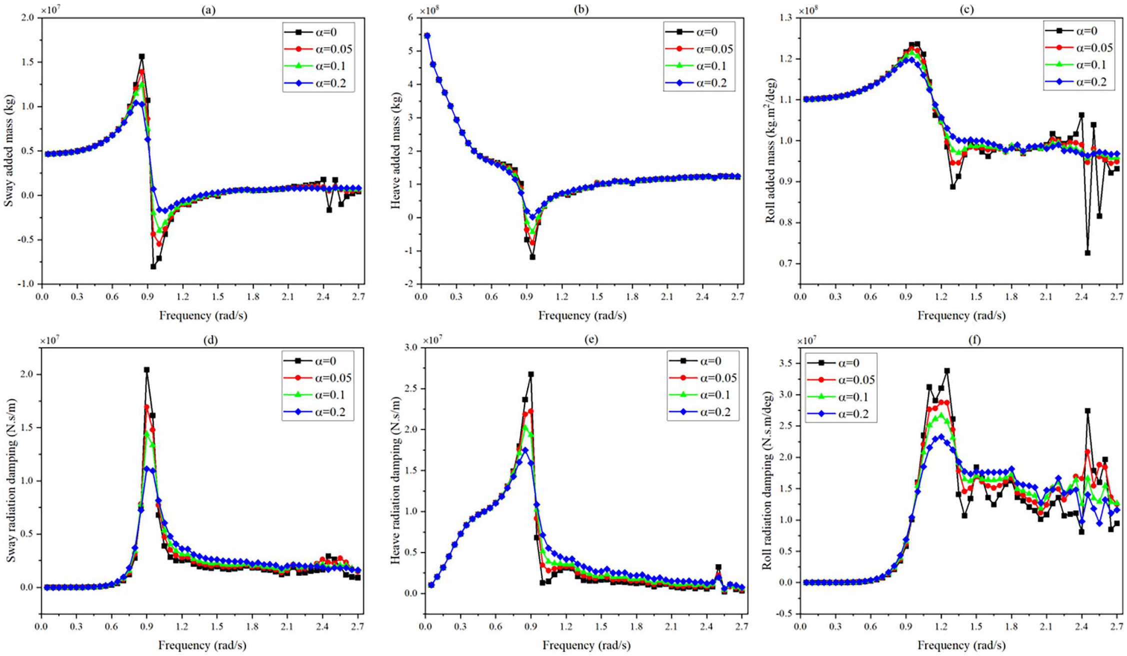

Figure 8: Hydrodynamic coefficients of the ship in sway, heave and roll DOFs with different damping factors

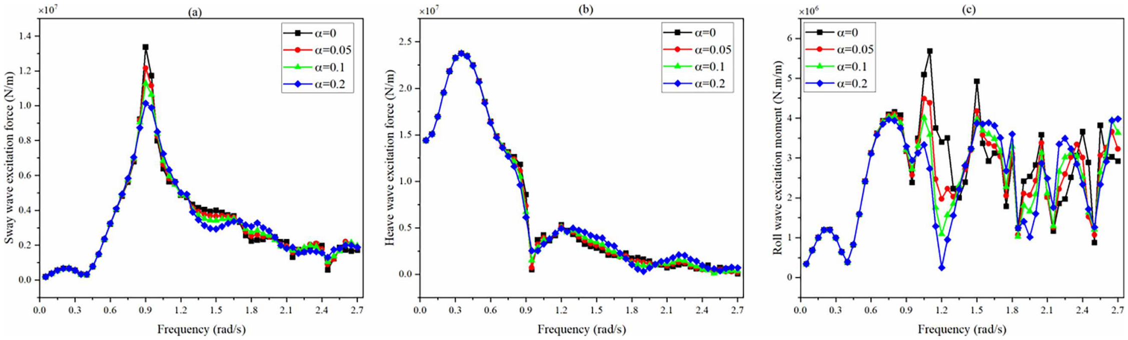

Figure 9: Wave forces of the ship in sway, heave and roll DOFs with different damping factors

After obtaining the relevant hydrodynamic coefficients and wave excitations, the sway, heave, and roll RAOs are computed using Eq. (14), as illustrated in Fig. 10. The figure indicates that the damping lid has negligible influence on the sway RAO, whereas for the heave and roll motions, slight damping effects are observed near a frequency of approximately 1.2 rad/s. This behavior contrasts with the more evident damping trends observed in the hydrodynamic coefficients and wave excitations. In the following subsection, RAO-based time-domain responses are used to determine an appropriate damping factor. It should also be noted that the accuracy of time-domain motion responses obtained using the Cummins model can be validated against frequency-domain RAOs under free-floating conditions.

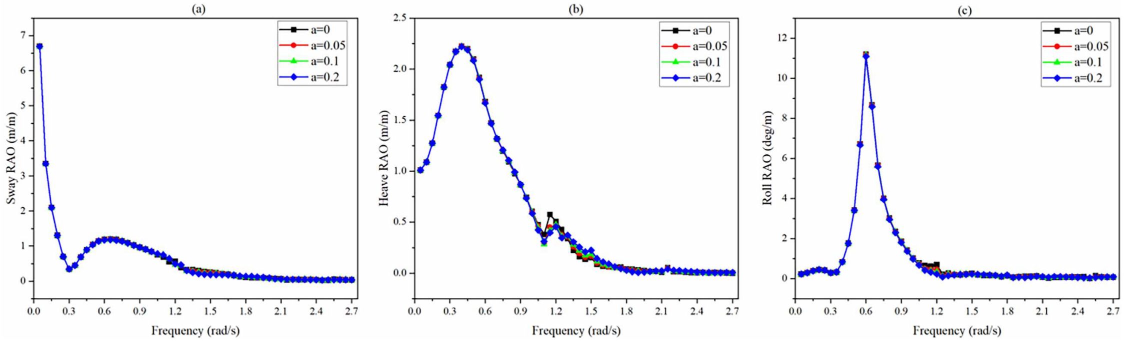

Figure 10: RAOs of the ship in sway, heave and roll DOFs with different damping factors

5.3 Determination of the Damping Factor

Due to narrow-gap resonance, the hydrodynamic coefficients and wave excitation forces of the ship exhibit abrupt variations near the resonance frequencies. Under such conditions, the retardation function may converge slowly or even fail to converge, which can introduce errors into the time-domain response. Therefore, it is necessary to determine an appropriate damping factor to ensure reliable estimates. Based on Eq. (26), Fig. 11 illustrates the retardation functions for the sway, heave, and roll degrees of freedom (DOFs). The figure indicates that higher damping factors lead to faster convergence of the retardation functions. Under these conditions, the potential errors caused by hydrodynamic interactions can be evaluated by comparing the RAO-based responses with those obtained from the Cummins model [33].

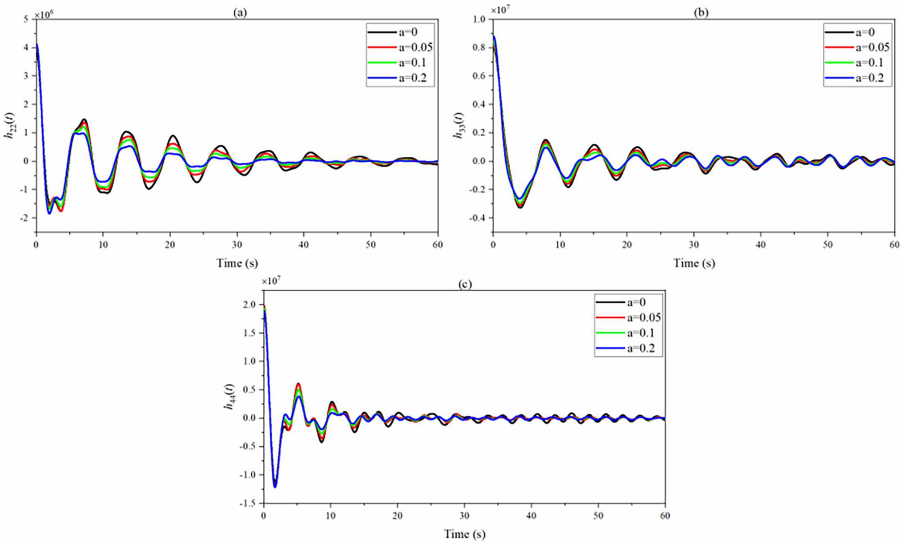

Figure 11: Comparisons of $h(t)$ of the ship in sway, heave and roll DOFs with different damping factor

Two frequencies near the piston-mode natural frequency, $\omega = 0.85$ and $\omega = 1.2$ rad/s, are selected for further analysis, as both induce oscillatory behavior in the hydrodynamic properties and are notably influenced by the damping factor, as inferred in Figs. 8 and 9. Time-domain simulations are then performed for a free-floating ship subjected to regular waves with $\beta = 90^\circ$, $A_\omega = 0.125$ m, and $\omega = 0.85$ and 1.2 rad/s. Figs. 12 and 13 compare the heave and roll responses obtained using various damping factors between the RAO-based method and the retardation-function approach. As shown in these figures, when the damping factor is less than 0.2, noticeable discrepancies appear in both amplitude and phase for the heave responses between the two approaches. In contrast, for the roll motion, the phase agreement remains consistent across both frequency conditions. Moreover, when $\omega = 0.85$ rad/s and $\alpha = 0.2$, the heave and roll motion responses exhibit excellent agreement between the RAO-based and retardation-function-based results. At $\omega = 1.2$ rad/s, however, a damping factor larger than 0.05 is required to achieve a comparable level of agreement. It is important to emphasize that selecting an excessively large damping factor is not physically meaningful. Instead, the damping factor should be carefully chosen for each specific condition to effectively suppress oscillations in the hydrodynamic characteristics while minimizing errors introduced by the retardation function in the Cummins model [33]. The objective is to achieve a reasonable, rather than excessive, level of viscous correction. Based on the above analysis, the suitable damping factors for $\omega = 0.85$ and $\omega = 1.2$ rad/s are determined to be 0.2 and 0.1, respectively.

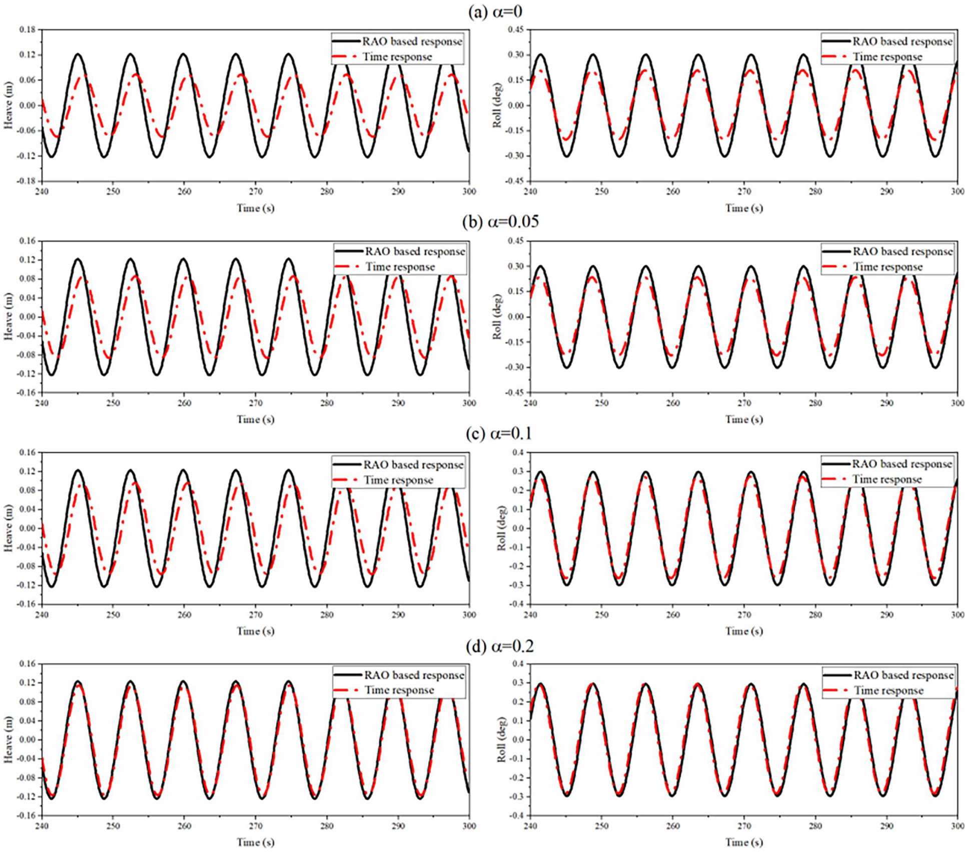

Figure 12: Comparisons of heave and roll responses between the RAO-based and retardation-based responses with different damping factors under $\omega = 0.85$ rad/s

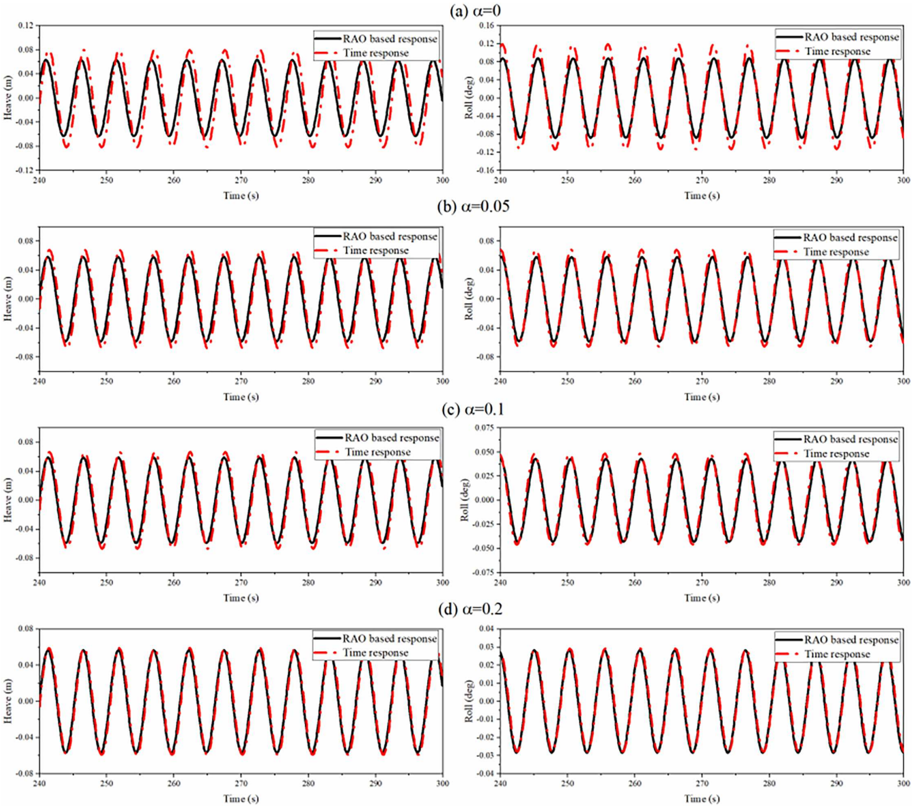

Figure 13: Comparisons of heave and roll response between the RAO-based and retardation-based responses with different damping factors under $\omega = 1.20$ rad/s

5.4 Extreme Loads of Mooring Lines and Fenders

For the two wave frequencies examined in the previous subsection, the corresponding harsh sea states are defined based on the conditions at the operational site. For the first sea state, associated with $\omega = 0.85$ rad/s, the significant wave height is 0.3 m, and the wind and current velocities are 10 and 0.2 m/s, respectively. For the second sea state, corresponding to $\omega = 1.2$ rad/s, the significant wave height is 0.6 m, while the wind and current velocities are 15 and 0.3 m/s, respectively. In both cases, the incident direction is 90°.

To ensure the safety of the mooring system under severe ocean conditions, it is necessary to evaluate the extreme loads acting on all mooring lines and fenders. For each sea state, 20 random sub-states with different wave seeds are generated, and each time-domain simulation is performed over a duration of 3 h. From the time histories of each simulation, the maximum mooring line tension and fender reaction force are extracted. Subsequently, the Gumbel distribution is employed to fit the extracted maxima and estimate the short-term extreme responses. The corresponding expression for the Gumbel distribution is given as follows:

$$F_X(x) = \exp\left[-\exp\left(\frac{x-\lambda}{\mu}\right)\right] \tag{32}$$

where: F represents the non-exceedance probability; X is the random variable; x is the independent variable; λ and μ are the position and scale parameters of the Gumbel distribution, respectively.

To determine the short-term extreme response, the linear fitting method is commonly applied to the Gumbel distribution. Therefore, the above expression is rearranged into the following linear form:

$$-\operatorname{In}\left[-\operatorname{In}F_X(x)\right]=\frac{1}{\mu}x-\frac{\lambda}{\mu} \tag{33}$$

During the fitting process, the maximum load values obtained from the 20 sub-cases are first arranged in ascending order and plotted along the x-axis. Their corresponding values of $-\operatorname{In}\left[-\operatorname{In}F_X(x)\right]$ are then calculated using the empirical formula and plotted on the y-axis. Finally, the least-squares method is applied to determine the optimal linear fitting curve. Based on the obtained λ and μ parameters, the short-term extreme response is defined as the x-value corresponding to a 95% non-exceedance probability.

Figs. 14 and 15 present the Gumbel distribution fitting results for the extreme loads of six mooring lines and two fenders under the two harsh sea states, respectively. According to the fitted results, Line #1, located at the bow, experiences the highest load, while Line #5, positioned at the stern, exhibits the lowest load. For the fenders, the one located near the bow is subjected to a higher contact force than the one near the stern. Table 4 summarizes the extreme load values of all mooring lines and fenders for each sea state, along with their corresponding safety factors. According to Refs. [46,47], the safety factor for both mooring lines and fenders is 1.67. The results listed in Table 4 indicate that the mooring system remains within safe limits under both harsh sea states.

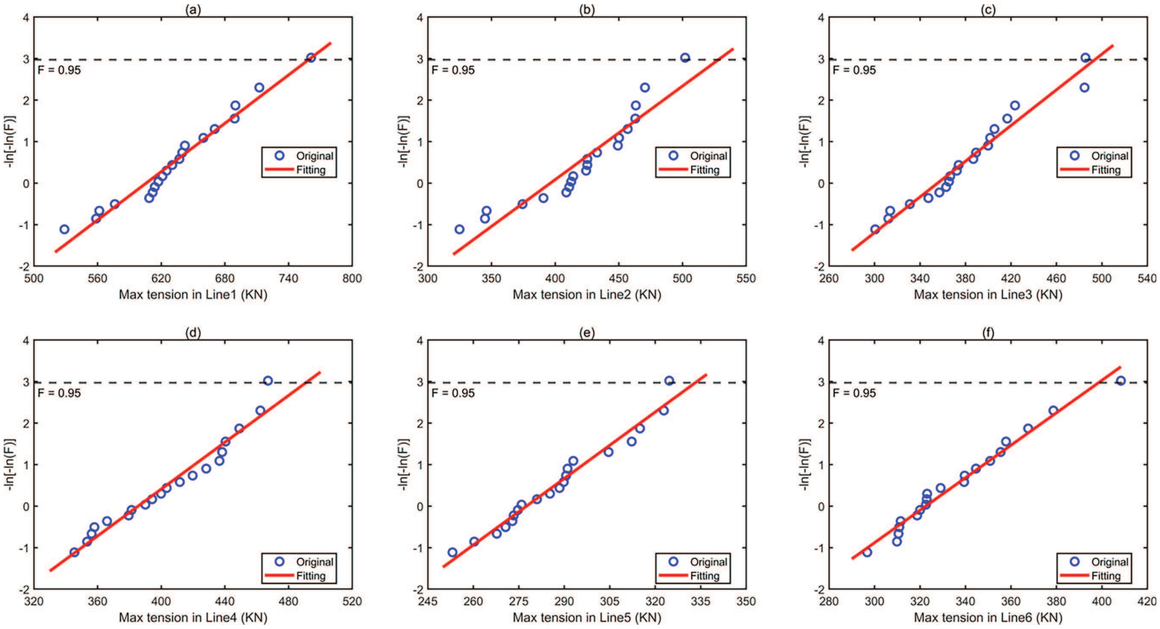

Figure 14: (Continued)

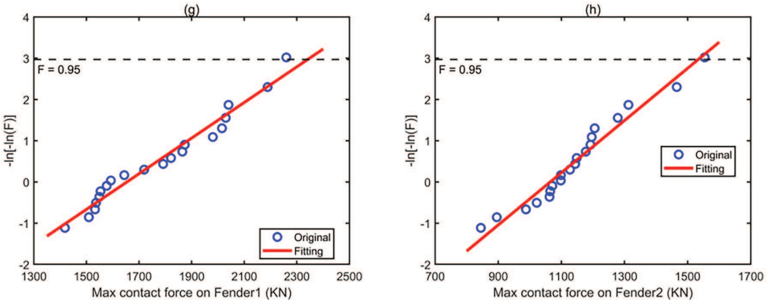

Figure 14: Fitted Gumbel distributions of extreme loads of mooring lines and fenders under severe sea condition 1

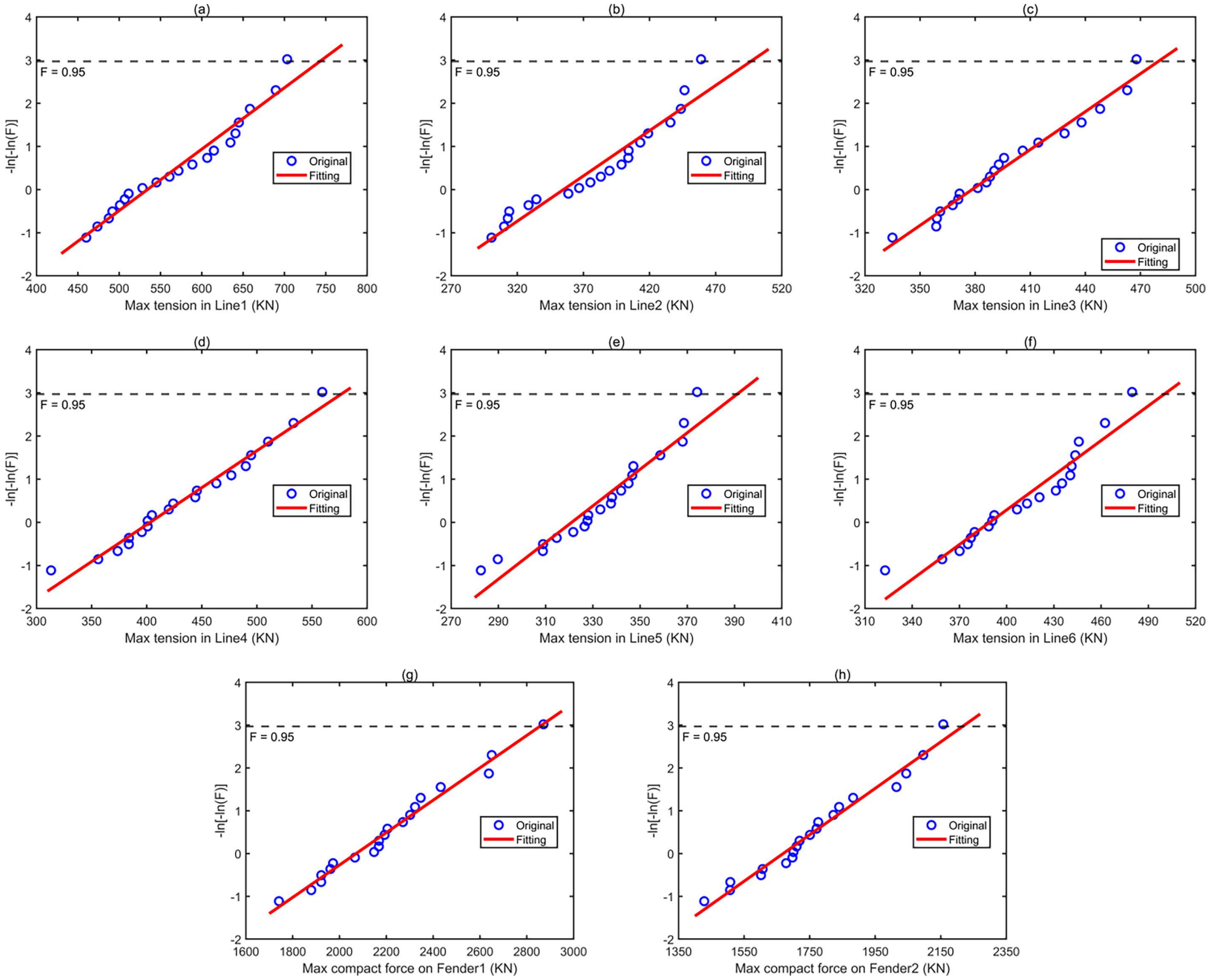

Figure 15: Fitted Gumbel distributions of extreme loads of mooring lines and fenders under under severe sea condition 2

Table 4: Short-term extreme loads of lines and fenders

	Severe sea condition 1		**Severe sea condition 2**	
	Extreme response (kN)	**Safety factor**	**Extreme response (kN)**	**Safety factor**
Line #1	758.836	2.15	742.765	2.20
Line #2	528.106	3.10	496.479	3.30
Line #3	493.630	3.32	479.698	3.41
Line #4	490.800	3.33	576.427	2.84
Line #5	333.186	4.91	391.062	4.19
Line #6	398.461	4.11	500.083	3.27
Fender #1	2341.1	2.09	2855.3	1.71
Fender #2	1533.6	3.19	2216.5	2.21

6 Conclusions

This study investigates the hydrodynamic interactions and the application of the damping lid method in an engineering ship–dock berthing system. The hydrodynamic characteristics are evaluated using three-dimensional potential flow theory combined with the boundary element method (BEM), while the time-domain dynamic responses are computed based on the Cummins model. Because the potential flow model does not account for viscous damping, the damping lid method is employed to suppress the abrupt variations in hydrodynamic coefficients and wave excitation forces around resonance frequencies. After validating the method, appropriate damping factors are determined for two specific wave frequencies. Finally, the extreme loads and safety assessments of the mooring lines and fenders are conducted. Based on the simulation results, the following key conclusions are drawn:

1. In the absence of viscous damping correction, the hydrodynamic properties of the ship exhibit significant oscillations near resonance frequencies. Furthermore, narrower gaps between the ship and dock lead to stronger hydrodynamic interactions. In addition to the piston mode, sloshing modes appear in cases with larger gap widths.
2. The damping lid method demonstrates a clear attenuation effect across various damping factors. For $\omega = 0.85$ and $\omega = 1.2$ rad/s, comparisons between time-domain responses based on frequency-domain RAOs and the Cummins equation yield optimal damping factors of 0.2 and 0.1, respectively.
3. Under the two harsh sea states, the short-term extreme loads on the mooring lines and fenders are estimated using the Gumbel distribution with linear fitting. The calculated safety factors remain below the allowable threshold, indicating that the mooring system maintains adequate safety under both conditions.

However, this study has certain limitations. To achieve more accurate viscous damping corrections, experimental studies or CFD simulations should be conducted, as wave elevations within narrow gaps tend to be more sensitive to the damping factor than the overall ship motion responses. In addition, only a single incident direction of environmental loading is considered in the time-domain analysis, whereas in real-world scenarios, the directions of waves, wind, and currents may differ. These limitations should be addressed in future work.

Finally, future research will also focus on examining how variations in narrow-gap configurations influence hydrodynamic interactions, and based on the findings, propose practical recommendations for determining optimal berthing distances in engineering applications.

Acknowledgement: The corresponding author would like to thank Siqi Wu for the patience, care and support over the past years.

Funding Statement: This paper was supported by National Natural Science Foundation of China (No. 52471284), Jiangsu Province "Qinglan Project" Outstanding Young Backbone Teacher Training Program, Lianyungang City "521 Project" Scientific Research Funding Program (No. LYG065212024049), and MTIC-JUST Joint Innovation Center Development Fund (No. 2025MTIC-JUST003).

Author Contributions: Conceptualization, Haitao Wu; methodology, Haitao Wu; simulation, Zhiyang Zhang; data curation, Zhiyang Zhang; visualization, Zhiyang Zhang; validation, Zhiyang Zhang; formal analysis, Zhiyang Zhang, Xingyu Pan and Ziheng Wang; writing—original draft preparation, Zhiyang Zhang; funding acquisition, Zhiyang Zhang and Weixing Liu; writing—review and editing, Weixing Liu and Haitao Wu; supervision, Haitao Wu. All authors reviewed the results and approved the final version of the manuscript.

Availability of Data and Materials: The authors confirm that the data supporting the findings of this study are available within the article.

Ethics Approval: Not applicable.

Conflicts of Interest: The authors declare no conflicts of interest to report regarding the present study.

References

1. Sande J, Figuero A, Tarrío-Saavedra J, Peña E, Alvarellos A, Rabuñal JR. Application of an analytic methodology to estimate the movements of moored vessels based on forecast data. Water. 2019;11(9):1841. doi:10.3390/w11091841.
2. Sasa K, Incecik A. Numerical simulation of anchored ship motions due to wave and wind forces for enhanced safety in offshore harbor refuge. Ocean Eng. 2012;44(1):68–78. doi:10.1016/j.oceaneng.2011.11.006.
3. Liu BJ, Chen XY, Zhang YQ, Xie J, Chang J. Influence of regular wave and ship characteristics on mooring force prediction by data-driven model. China Ocean Eng. 2020;34(4):589–96. doi:10.1007/s13344-020-0053-1.
4. Paulauskas V, Paulauskas D, Wijffels J. Ship safety in open ports. Transport. 2009;24(2):113–20. doi:10.3846/1648-4142.2009.24.113-120.
5. Shen W, Hu J, Liu L, Chen H. Operability analysis and line failure risk assessment for a tanker moored at berth. Ocean Eng. 2024;300:117439. doi:10.1016/j.oceaneng.2024.117439.
6. Ziylan K, Nas S. A quasi-static mooring analysis approach for berthed ships. Ocean Eng. 2024;309:118488. doi:10.1016/j.oceaneng.2024.118488.
7. Wen H, Zhu G, Ren B, Chang X, Wu J, Wang Y. Experimental study of multi-buoy-assisted moored ship motion at open berth. Mar Struct. 2023;92:103496. doi:10.1016/j.marstruc.2023.103496.

8. Wan L, Han M, Jin J, Zhang C, Magee AR, Hellan Ø, et al. Global dynamic response analysis of oil storage tank in finite water depth: focusing on fender mooring system parameter design. Ocean Eng. 2018;148:247–62. doi:10.1016/j.oceaneng.2017.11.021.
9. Yan MY, Ma XZ, Zheng ZJ, Dong GH. Numerical research on motion characteristics of a large container ship moored at a port under swell. Ocean Eng. 2023;41(6):100–11. (In Chinese). doi:10.16483/j.issn.1005-9865.2023.06.010.
10. Zhu Y, Li X, Zhu Y, Wen M, Chen H, Yu X, et al. Experimental and numerical investigation of dynamic characteristics and safe mooring criteria of moored outfitting ships under swell conditions. Ocean Eng. 2024;314:119771. doi:10.1016/j.oceaneng.2024.119771.
11. Molin B. On the piston and sloshing modes in moonpools. J Fluid Mech. 2001;430:27–50. doi:10.1017/s0022112000002871.
12. Gao J, Chen H, Zang J, Chen L, Wang G, Zhu Y. Numerical investigations of gap resonance excited by focused transient wave groups. Ocean Eng. 2020;212:107628. doi:10.1016/j.oceaneng.2020.107628.
13. Li B. Multi-body hydrodynamic resonance and shielding effect of vessels parallel and nonparallel side-by-side. Ocean Eng. 2020;218:108188. doi:10.1016/j.oceaneng.2020.108188.
14. Shu L, Bin T. Fluid resonance between twin floating barges with roll motion under wave action. China Ocean Eng. 2021;35(6):789–801. doi:10.1007/s13344-021-0070-8.
15. Zhang D, Du J, Yuan Z, Yu S, Li H. Motion characteristics of large arrays of modularized floating bodies with hinge connections. Phys Fluids. 2023;35(7):077107. doi:10.1063/5.0153317.
16. Lewandowski EM. Multi-vessel seakeeping computations with linear potential theory. Ocean Eng. 2008;35(11–12):1121–31. doi:10.1016/j.oceaneng.2008.04.011.
17. Moradi N, Zhou T, Cheng L. Effect of inlet configuration on wave resonance in the narrow gap of two fixed bodies in close proximity. Ocean Eng. 2015;103:88–102. doi:10.1016/j.oceaneng.2015.04.063.
18. Saitoh T, Seto T, Miao G, Ishida H. Characteristics and appearance condition of fluid resonance in a narrow gap between modules of very large floating structure. Proc Civ Eng Ocean. 2004;20:1317–22. doi:10.2208/prooe.20.1317.
19. Faltinsen OM, Rognebakke OF, Timokha AN. Two-dimensional resonant piston-like sloshing in a moonpool. J Fluid Mech. 2007;575:359–97. doi:10.1017/s002211200600440x.
20. Chua K, de Mello P, Malta E, Vieira D, Watai R, Ruggeri F, et al. Irregular seas model experiments on side-by-side barges. In: Proceedings of the 28th International Ocean and Polar Engineering Conference; 2018 Jun 10–15; Sapporo, Japan.
21. Chua KH, de Mello PC, Nishimoto K, Choo YS. Model experiments of floating side-by-side barges. In: Volume 9: Rodney Eatock Taylor Honoring Symposium on Marine and Offshore Hydrodynamics; Takeshi Kinoshita Honoring Symposium on Offshore Technology; 2019 Jun 9–14; Glasgow, UK. p. V009T12A008. doi:10.1115/omae2019-95238.
22. Jiang SC, Bai W, Tang GQ. Numerical simulation of wave resonance in the narrow gap between two non-identical boxes. Ocean Eng. 2018;156:38–60. doi:10.1016/j.oceaneng.2018.02.055.
23. Sun JY, Xu YW, Fu SX, Zhao B, Song B, Zhang MM, et al. Investigation on the Fishtailing motion of a single chain mooring aquaculture ship under the actions of wind and current. Ocean Eng. 2023;41(5):48–56,69. (In Chinese). doi:10.16483/j.issn.1005-9865.2023.05.005.
24. Huijsmans R, Pinkster J, De Wilde J. Diffraction and radiation of waves around side-by-side moored ships. In: Proceedings of the 11th International Offshore and Polar Engineering Conference; 2001 Jun 17–22; Stavanger, Norway.
25. Newman J. Progress in wave load computations on offshore structures. In: Proceedings of the 23rd International Conference on Offshore Mechanics & Arctic Engineering (OMAE); 2004 Jun 20–25; Vancouver, BC, Canada.

26. Chen X. Hydrodynamic analysis for offshore LNG terminals. In: Proceedings of the 2nd International Workshop on Applied Offshore Hydrodynamics; 2005 Apr 14–15; Rio de Janeiro, Brazil.
27. Zhao W, Pan Z, Lin F, Li B, Taylor PH, Efthymiou M. Estimation of gap resonance relevant to side-by-side offloading. Ocean Eng. 2018;153(2):1–9. doi:10.1016/j.oceaneng.2018.01.056.
28. Watai RA, Dinoi P, Ruggeri F, Souto-Iglesias A, Simos AN. Rankine time-domain method with application to side-by-side gap flow modeling. Appl Ocean Res. 2015;50:69–90. doi:10.1016/j.apor.2014.12.002.
29. Liu H, Chen M, Han Z, Zhou H, Li L. Feasibility study of a novel open ocean aquaculture ship integrating with a wind turbine and an internal turret mooring system. J Mar Sci Eng. 2022;10(11):1729. doi:10.3390/jmse10111729.
30. Barltrop N. Floating structures: a guide for design and analysis. Vol. 1. Cupertino, CA, USA: CMPT and OPL; 1998.
31. Newman JN. The theory of ship motions. Adv Appl Mech. 1979;18:221–83. doi:10.1016/S0065-2156(08)70268-0.
32. Chen M, Ouyang M, Li T, Zou M, Ye J, Tian X. Numerical modelling of a catamaran float-over deck installation for a spar platform with complex hydrodynamic interactions and mechanical couplings. Ocean Eng. 2023;287:115905. doi:10.1016/j.oceaneng.2023.115905.
33. Chen M, Yuan G, Li B, Li CB, Ouyang M, Li L, et al. Dynamic analysis of lift-off operation of offshore wind turbine jacket foundation from the transportation barge. Ocean Eng. 2024;301:117443. doi:10.1016/j.oceaneng.2024.117443.
34. Saitoh T, Miao GP, Ishida H. Theoretical analysis on appearance condition of fluid resonance in a narrow gap between two modules of very large floating structure. In: Proceedings of the 3rd Asia-Pacific Workshop on Marine Hydrodynamics; 2006 Jun 27–28; Shanghai, China.
35. Newman JN. Wave effects on multiple bodies. In: Kashiwagi M, editor. Hydrodynamics in ship and ocean en-gineering. Fukuoka City, Japan: Kyushu University; 2001.
36. Pinkster JA. Low-frequency phenomena associated with vessels moored at sea. Soc Petrol Eng J. 1975;15(6):487–94. doi:10.2118/4837-pa.
37. Havelock TH. Waves due to a floating sphere making periodic heaving oscillations. Proc R Soc Lond A. 1955;231(1184):1–7. doi:10.1098/rspa.1955.0152.
38. Hess JL, Smith AMO. Calculation of nonlifting potential flow about arbitrary three-dimensional bodies. J Ship Res. 1964;8(4):22–44. doi:10.5957/jsr.1964.8.4.22.
39. Cummins WE. The impulse response function and ship motions. Schiffstechnik. 1962;9:101–9.
40. Ogilvie TF. Recent progress toward the understanding and prediction of ship motions. In: Ship motions and drag reduction. Washington, DC, USA: Office of Naval Research; 1966.
41. ANSYS Inc. ANSYS AQWA theory manual. Canonsburg, PA, USA: ANSYS Inc.; 2023.
42. Wu H, Deng W, Yuan Z. Effects of short-crestedness and currents on the dynamic response of a floating wave-energy harvesting platform. Phys Fluids. 2025;37(3):037202. doi:10.1063/5.0264487.
43. Xu X, Yang JM, Li X, Xu L. Hydrodynamic performance study of two side-by-side barges. Ships Offshore Struct. 2014;9(5):475–88. doi:10.1080/17445302.2014.889368.
44. Yue M, Liu Q, Li C, Ding Q, Cheng S, Zhu H. Effects of heave plate on dynamic response of floating wind turbine Spar platform under the coupling effect of wind and wave. Ocean Eng. 2020;201:107103. doi:10.1016/j.oceaneng.2020.107103.
45. Zou M, Chen M, Zhu L, Li L, Zhao W. A constant parameter time domain model for dynamic modelling of multi-body system with strong hydrodynamic interactions. Ocean Eng. 2023;268:113376. doi:10.1016/j.oceaneng.2022.113376.

46. DNV-OS-E301. Position mooring. Høvik, Norway: DNV; 2004.
47. Xu X, Sahoo P, Evans J, Tao Y. Hydrodynamic performances of FPSO and shuttle tanker during side-by-side offloading operation. Ships Offshore Struct. 2019;14(sup1):292–9. doi:10.1080/17445302.2019.1580845.